RESEARCH ARTICLE | MARCH 26 2025

# Single- vs dual-source vapor deposition of inorganic halide perovskites: A case study of CsPbBr<sub>3</sub>

Tomáš Musálek <sup>(1)</sup>; Petr Liška <sup>(1)</sup>; Amedeo Morsa <sup>(1)</sup>; Jon Ander Arregi <sup>(1)</sup>; Pavel Klok <sup>(1)</sup>; Matouš Kratochvíl <sup>(1)</sup>; Dmitry Sergeev <sup>(1)</sup>; Michael Müller <sup>(1)</sup>; Tomáš Šikola <sup>(1)</sup>; Miroslav Kolíbal <sup>12</sup>



APL Mater. 13, 031118 (2025) https://doi.org/10.1063/5.0242134





# Articles You May Be Interested In

Vapor deposition of CsPbBr3 thin films by evaporation of CsBr and PbBr2

J. Vac. Sci. Technol. A (June 2021)

Interface engineering of  $CsPbBr_3/TiO_2$  heterostructure with enhanced optoelectronic properties for all-inorganic perovskite solar cells

Appl. Phys. Lett. (February 2018)

Combining SSVD and subsequent heat treatment processes to fabricate high-quality CsPbBr<sub>3</sub> perovskite films

J. Appl. Phys. (October 2024)





# Single- vs dual-source vapor deposition of inorganic halide perovskites: A case study of CsPbBr<sub>3</sub>

Cite as: APL Mater. 13, 031118 (2025); doi: 10.1063/5.0242134 Submitted: 2 October 2024 • Accepted: 5 March 2025 •

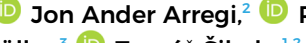






Published Online: 26 March 2025









# **AFFILIATIONS**

- <sup>1</sup> Institute of Physical Engineering, Brno University of Technology, Technická 2, 61669 Brno, Czech Republic
- <sup>2</sup>CEITEC BUT, Brno University of Technology, Purkyňova 123, 61200 Brno, Czech Republic
- <sup>3</sup>Institute of Energy Materials and Devices, Structure and Properties of Materials (IMD-1), Forschungszentrum Jülich, 52425 Jülich, Germany
- Materials Research Centre, Faculty of Chemistry, Brno University of Technology, Purkyňova 118, 61200 Brno, Czech Republic
- <sup>5</sup>NETZSCH-Gerätebau GmbH, Selb D-95100, Germany

# **ABSTRACT**

Inorganic halide perovskites have become attractive for many optoelectronic applications due to their outstanding properties. While chemical synthesis techniques have been successful in producing high-quality perovskite crystals, scaling up to wafer-scale thin films remains challenging. Vapor deposition methods, particularly physical vapor deposition and chemical vapor deposition, have emerged as potential solutions for large-scale thin film fabrication. However, the control of phase purity during deposition remains problematic. Here, we investigate singlesource (CsPbBr<sub>3</sub>) and dual-source (CsBr and PbBr<sub>2</sub>) physical vapor deposition techniques with the aim of achieving phase-pure CsPbBr<sub>3</sub> thin films. Utilizing Knudsen effusion mass spectrometry, we demonstrate that while the single-source CsPbBr3 evaporation is partially congruent, it leads to compositional changes in the evaporant over time. The dual-source evaporation, with a precise control of the PbBr<sub>2</sub>/CsBr flux ratio, can improve phase purity, particularly at elevated substrate temperatures under excess PbBr2 conditions. Our results give direct evidence that the growth is CsBr-limited. Overall, our findings provide critical insights into the vapor phase deposition processes, highlighting the importance of evaporation conditions in achieving the desired inorganic perovskite stoichiometry and morphology.

© 2025 Author(s). All article content, except where otherwise noted, is licensed under a Creative Commons Attribution (CC BY) license (https://creativecommons.org/licenses/by/4.0/). https://doi.org/10.1063/5.0242134

# I. INTRODUCTION

Inorganic halide perovskites have received tremendous and still increasing attention from the scientific community because of their excellent optoelectronic properties, which qualify them for use in solar cells, light-emitting diodes, x-ray detectors, and more. This rapid burst of scientific studies was fueled mainly by chemical synthesis preparation techniques, which provide high-quality perovskite (nano)crystals at very low costs.<sup>3</sup> However, upscaling this approach to wafer-scale thin films poses a great challenge. Recently, vapor deposition techniques have come to focus; evaporation from

a solid source under vacuum conditions is an established technology, e.g., in semiconductor lasers, allowing the preparation of thin films with atomic-scale precision.4 Building on a large know-how from different material systems, deposition from a vapor phase has the potential to become a dominant technology for a large-scale deposition of inorganic halide perovskite thin films as well.

The perovskite preparation technique is vital to determine the relevant properties of the resultant thin film.<sup>5</sup> Many experimental studies on vapor deposition of halide perovskites have been recently summarized by timely and important reviews.<sup>6-8</sup> Importantly, if

a) Author to whom correspondence should be addressed: kolibal.m@fme.vutbr.cz

22 September 2025 11:35:09

effusion cells are utilized, vapor deposition offers much better control of the evaporation fluxes, thus allowing for the engineering of the grain size<sup>9,10</sup> or the intermixing of different chalcogenides. <sup>11</sup> The efficacy of vapor deposition has soon been recognized and demonstrated by the deposition of the perovskite solar cells<sup>12</sup> and the perovskite light emitting diodes. <sup>13,14</sup> However, many issues prevail. Deposition of CsPbBr<sub>3</sub> by evaporation of precursors of different compositions results in thin films of CsPbBr<sub>3</sub> mixed with unreacted CsBr and PbBr<sub>2</sub> or other phases of a different stoichiometries. Hence, the phase-purity control is poor even for the most prominent inorganic halide perovskite, CsPbBr<sub>3</sub>. Overall, the literature reviews give a clear picture of current know-how in the field: a comprehensive understanding of the processes involved in every stage of the growth (evaporation, transport, and growth) is lacking. <sup>6–8</sup>

The most prominent approaches to vacuum-based vapor deposition are chemical vapor deposition (CVD) and evaporation from Knudsen-like cells, the latter belonging to the family of physical vapor deposition (PVD) techniques. Usually, CVD relies on tubular quartz reactors, where, for instance, the precursor powders are placed at a certain position within a temperature gradient across the furnace. The vaporized precursors are dragged by a carrier gas toward the substrate, which is located at different positions within the tube furnace; here, the vapors condense into a thin layer. A sealed variant of CVD (without the carrier gas) is called the chemical vapor transport (CVT); here, the sample size is limited. Tubular quartz CVD and CVT reactors that utilize solid precursors are mostly single-use; after each growth run, the precursors need to be refilled. Only recently, experimental CVD setups for perovskite growth that do not require frequent precursor refilling were introduced. 15,16 In contrast to tubular quartz CVD, PVD techniques are typically housed in larger high-vacuum apparatus,8 where the Knudsen cells do not require refilling after every deposition, thus ideally providing stable and reproducible growth runs. However, achieving this is typically difficult in perovskite growth, as is shown in this paper.

Most often, the precursors in Knudsen cells are located in resistively heated crucibles. Another possibility, specifically for organic–inorganic perovskites, is the pulsed laser deposition (PLD)<sup>17</sup> or its variant, resonant infrared matrix-assisted pulsed laser evaporation (RIR-MAPLE).<sup>18</sup> These technologies seem very promising but remain unexplored.

Regardless of the technology in use, the deposition of multicomponent materials is performed from individual precursors of each component placed separately in different heating zones<sup>19</sup> or separate evaporation cells, <sup>20–22</sup> as well as from a single precursor. 11,23,24 The former approach promises a good stoichiometry control of the resulting material via tuning the evaporation fluxes of each constituent (e.g., CsBr and PbBr<sub>2</sub>). Certainly, most studies focused on finding the optimum evaporation flux ratio. With rare exceptions,<sup>28</sup> depositing two constituents at a 1:1 evaporation flux ratio does not lead to stoichiometry preservation of the deposit (CsBr + PbBr<sub>2</sub> = CsPbBr<sub>3</sub>). The on-surface growth is determined by kinetic processes, schematically illustrated in Fig. 1, that significantly alter the individual surface concentrations of the species involved.<sup>29,30</sup> These processes are thermally activated and follow Boltzmann statistics. Typically, high diffusivity at the surface is a key factor for the deposited atoms and molecules to reach low-energy positions.<sup>31</sup> If multicomponent materials are deposited, one ideally needs a high diffusivity and similar desorption rate of all

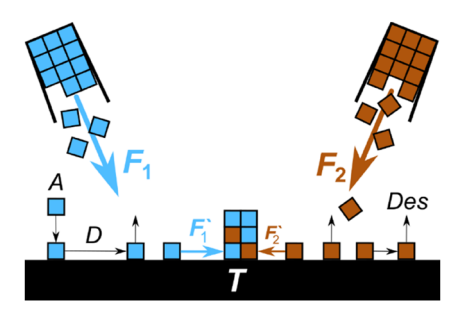


**FIG. 1.** Schematic illustration of the processes involved in multicomponent deposition. In this case, two evaporation sources (blue and brown) of different constituents (blue and brown bricks) are evaporated at the same evaporation rates F, i.e.,  $F_1 = F_2$ . Nevertheless, the on-surface fluxes,  $F_1{}' > F_2{}'$ , are not equal due to different kinetic rates of on-surface processes for each constituent (A – adsorption, D – diffusion, Des – desorption). The kinetic rates are significantly dependent on sample temperature T. Hence, the growth may not result in stoichiometric product, and the initial 1:1 ratio of the evaporation fluxes  $F_1$  and  $F_2$  is not preserved on the surface.

constituents simultaneously,  $^{\rm 32}$  which is usually not the case (despite the fact that, for example, the CsPbBr3 formation from gaseous CsBr and PbBr<sub>2</sub> is exothermic, -386 kJ/mol, <sup>13</sup> providing an additional thermal energy to deposited molecules). Such a situation is schematically illustrated in Fig. 1, where imbalance in the surface fluxes of individual constituents arises due to the enhanced desorption of one of the species. Specifically, for halide perovskites, a proposed solution to this issue involves a sequential, separate evaporation of each component, one after another, followed by annealing of the entire multilayer stack.<sup>33</sup> However, post-growth annealing is another critical step that faces several kinetic restrictions. Perfect mixing is achieved only if the temperature is high enough to promote interdiffusion while avoiding PbBr<sub>2</sub> desorption. An alternative approach could be the deposition of multiple layer sequences, but in principle, the difficulties associated with annealing persist.<sup>34</sup> In addition, issues arise outside of vacuum conditions due to varying levels of humidity.35

Hence, an important "turning knob" for optimizing the growth process and achieving the correct stoichiometry is the sample temperature  $T^{.29}$  The numerous surface processes are difficult to precisely control by only two variables (sample temperature and precursor fluxes). Nevertheless, it is possible to build on previously established compound semiconductor deposition processes, utilizing self-limited kinetics of the growth system. This is the case, e.g., of GaAs<sup>36</sup> and SnSe,<sup>37</sup> where the growth is Ga- and Sn-limited, respectively. The self-limiting conditions are achieved at elevated temperature under excess group V (or VI) precursor flux. High temperatures ensure that excess As (or Se) atoms are readily desorbed, leaving only those that form Ga-As (or Sn-Se) bonds and remain on the surface. Therefore, an optimum stoichiometric III-V crystal growth is achieved. Such an approach has not been studied for halide perovskites, as the knowledge of the surface processes that occur during growth from multiple precursor sources is rather limited.

Alternatively, evaporation from a single source (i.e., CsPbBr<sub>3</sub>) has the potential to simplify the phase-pure deposition, provided that the compound evaporates congruently. This means the composition of the vapor is reflecting that of the evaporant.<sup>38,39</sup> This is

possible if the precursor is in the form of a nanoscale powder or if the precursor pellet fragments into nanoscale parts and decomposes only after fragmentation.<sup>39</sup> The latter process has recently been documented to occur during the melting of CsPbBr<sub>3</sub>.<sup>40</sup> However, the congruent evaporation of CsPbBr3 has not yet been validated, despite speculations in the literature.<sup>26</sup> Understanding the singlesource evaporation of CsPbBr3 is complicated as different phases of the resulting perovskite layers are reported to be either Cs or Pb rich. 41,42 Post-growth alloying strategies have been employed to increase the purity of the CsPbBr<sub>3</sub> phase, <sup>25,41,42</sup> but this approach faces similar issues as the aforementioned annealing of multilayer stacks. 34,35 An apparent solution is the deposition at elevated temperature. Although this increases complexity, it simultaneously introduces the possibility of tuning the resulting morphology, from polycrystalline layers at lower temperatures to nanowires at higher temperatures, 19,24 although contradictory results have been reported so far.11

Here, we study single-source (CsPbBr<sub>3</sub>) and dual-source (CsBr and PbBr<sub>2</sub>) deposition strategies with the objective of depositing phase-pure CsPbBr3. We analyze two critical phases of growth by separately analyzing the evaporation products using Knudsen Effusion Mass Spectrometry (KEMS) and the growth products at different sample temperatures by relevant analytical techniques. We show that the decomposition of CsPbBr<sub>3</sub> is partially congruent; however, the precursor composition changes during the evaporation. It is observed that this problem can be resolved to some extent by elevating the sample temperature, which enhances the phase purity of the deposit by desorbing excess PbBr2. Similarly, the dual-source evaporation yields a high-purity CsPbBr3 evaporant at elevated sample temperatures because growth is CsBr-limited. At lower sample temperatures, other phases, namely CsPb2Br5 and Cs4PbBr6, are detected on the samples, either pure or mixed with CsPbBr<sub>3</sub>, CsBr, or PbBr<sub>2</sub>.

#### II. METHODS

Perovskite  $CsPbBr_3$  precursor synthesis:  $PbBr_2$  powder (Sigma-Aldrich, 99.999% purity) was dissolved in 48% aqueous HBr, and CsBr powder (Sigma-Aldrich, 99.999% purity) was dissolved in  $H_2O$ . In both cases, the molar ratio of the dissolved powders was 1:1. Next, the solutions were mixed, resulting in the precipitation of orange solid, which was suction filtered, washed with ethanol, and dried under vacuum. For co-evaporation experiments, pure  $PbBr_2$  and CsBr powders were used.

Perovskite evaporation: All evaporation experiments were conducted within a high vacuum (HV) chamber, maintaining a base pressure of  $1\times10^{-8}$  mbar. The chamber was equipped with two custom-built resistively heated effusion cells, both aligned at an incident angle of  $30^{\circ}$  relative to the substrate. During the operation, the pressure typically stabilized in the order of  $10^{-7}$  mbar. The evaporators were operated at  $450\,^{\circ}\mathrm{C}$  for the evaporation of single-source CsPbBr3 and in the range of 400--450 and  $240\text{--}360\,^{\circ}\mathrm{C}$  for the evaporation of CsBr and PbBr2, respectively. The evaporation rates were calibrated by a quartz crystal microbalance and validated on room-temperature deposited layers by step-height measurement by atomic force microscopy. The sample holder was fitted with a calibrated pyrolytic boron nitride (pBN) heater to ensure precise temperature control. Si(111) substrates were used in all the experiments.

X-ray diffraction (XRD): Structural analysis and phase identification of the deposited Cs-Pb-Br samples were performed via in-plane grazing incidence XRD (GIXRD) measurements and outof-plane specular diffraction using a Rigaku SmartLab (9 kW) diffractometer with Cu-K $\alpha$  radiation ( $\lambda = 1.54$  Å) and an incident parallel beam setting. A 5° in-plane Soller slit was utilized in both the incident and diffracted optics. For GIXRD, the x-ray source and the detector were set to a grazing angle ( $\omega = 0.8^{\circ}$ ,  $2\theta = 1.6^{\circ}$ ), and intensity profiles were acquired by scanning the  $2\theta/\chi$  angle, where the detector arm is laterally scanned in order to look for crystalline planes that are perpendicular to the sample surface. The grazingincidence measurement geometry maximizes the signal arising from the thin film in comparison to that of the substrate. In specific cases, we have also utilized the out-of-plane diffraction geometry (specular diffraction) by performing symmetric  $\theta$ -2 $\theta$  scans using a double-bounce Ge(022) monochromator, obtaining reflections from crystallographic planes parallel to the sample surface. Such a configuration allows scanning the  $2\theta$  angle with better resolution, which is necessary for discriminating between the orthorhombic and cubic CsPbBr3 phases. The recorded peaks were compared to crystallographic databases (see Fig. S1).

Scanning electron microscopy (SEM) was performed using Thermo Fisher Verios 450L and FEI Versa microscopes.

X-Ray Photoelectron Spectroscopy (XPS): Compositional analysis was performed using a Kratos Axis Supra XPS instrument utilizing the monochromated Al K $\alpha$  radiation (1486.6 eV) and a hemispherical analyzer set in a high magnification mode with a pass energy of 20 eV. The electron emission angle was set along the normal to the surface. All the spectra were acquired with an energy step of 0.05 eV. The perovskite phase analysis, presented in the supplementary material, was performed without shifting the spectra. Only to present the Pb $^0$  component clearly after prolonged x-ray irradiation, we have shifted the spectra shown in Fig. 6 with respect to the Pb $^{2+}$  component at 138.75 eV. $^{43}$  The intensity and fluence of the x-ray source were determined according to Ref. 44.

Photoluminescence and Raman spectroscopy analysis: Spectra were obtained using a Witec Alpha 300R confocal microscope setup with a built-in spectral camera and continuous wave laser illumination. The wavelength of the laser light used for excitation was 532 nm, and the optical power of the laser varied from 0.5 to 10 mW. The spectra were normalized with respect to the intensity of the Si Raman peak (520  $\rm cm^{-1}$ ). All the measurements were performed using an objective lens with  $100\times$  magnification, a 0.3 mm working distance, and a 0.9 numerical aperture. The diffraction grid settings for photoluminescence measurements and for the detailed Raman spectra observations were 600 and 1200 g/mm, respectively.

For time-resolved photoluminescence (TRPL) measurements, free space optics was used. The sample was placed into a Ø50 mm Thorlabs integration sphere with three SM05-threaded input ports and one SM05-threaded output port. The integration sphere has a reflectance greater than 94% over the wavelength range of 250–2500 nm. Through one SM05-threaded input port, excitation light from a pulsed laser diode (PIL 040-FS) with a 407 nm wavelength, 100 ps pulse width, 1.46 mW optical power, and 10 MHz repetition rate was directed onto the sample placed inside the integration sphere. The TRPL was collected through the SM05-threaded output port and directed to an avalanche photodiode (SPCM-AQRH-64, Excelitas Technologies). The measured

PL intensities were fitted with a single-exponential function as follows:

$$I(t) = I_0 \exp\left(-\frac{t}{\tau_1}\right),\tag{1}$$

where I(t) is the PL intensity at time t, whereas  $I_0$  and  $\tau_1$  are the amplitude and the lifetime of the charge transfer process.

For photoluminescence quantum yield measurements (PLQY), the same setup as for TRPL was used with some modifications. The excitation pulsed laser light, with a 407 nm wavelength, was operated at an optical power of 0.84 mW and a repetition rate of 20 MHz. The signal was collected through the SM05-threaded output port and directed to a Shamrock spectrograph 303i equipped with an iDus 420 CCD camera from Oxford Instruments, a diffraction grating of 150 g/mm, an input slit size of 10  $\mu$ m, and an integration time of 10 s. The PLQY was obtained and calculated as

$$\eta_{\text{PLQY}} = \frac{A_{\text{PL}}}{A_{\text{inc}} - A_{\text{scat}}} 100, \tag{2}$$

where  $A_{\rm PL}$  is the area under the photoluminescence curve,  $A_{\rm inc.}$  is the area under the reflectance curve of the bare substrate, and  $A_{\rm scat.}$  is the area under the reflectance curve of the substrate covered by the perovskite thin film.

Knudsen effusion mass spectrometry experiments were conducted using a FINNIGAN MAT 271 spectrometer at Forschungszentrum Jülich. Prior to sample introduction, the Knudsen cells were preconditioned by heating at 1000 °C for 12 h to remove impurities. For each measurement, ~40 mg of sample powder were loaded into the cell. Ionization was performed using an electron beam generated by a tungsten cathode, operating at an energy of 60–70 eV and an emission current of 0.47 mA. Two types of measurement series were carried out: isothermal measurements, where vapor species were analyzed at a constant temperature over time, and polythermal measurements, which were taken at different temperature intervals. Full experimental details are provided in the supplementary material.

# III. RESULTS

The species evaporated from the source materials are the building blocks for further perovskite phase formation on the substrate. We have utilized KEMS to identify the evaporated species from the single-source (CsPbBr3 pellet) as well as dual-source precursor(s) (CsBr and PbBr<sub>2</sub> powders). Figure 2 shows a mass spectrum recorded for each of these source materials heated to the temperatures further used in this study: CsPbBr<sub>3</sub> at 450 °C [Fig. 2(a)], CsBr at 450 °C [Fig. 2(b)], and PbBr<sub>2</sub> at 300 °C [Fig. 2(c)]. As expected, the CsPbBr<sub>3</sub> KEMS spectrum contains ions that do not appear in the spectra of CsBr or PbBr<sub>2</sub> alone, including CsPbBr<sub>2</sub><sup>+</sup> (493-503) m/z), which results from the fragmentation of CsPbBr<sub>3</sub> molecules after ionization. Although the fragmentation is very efficient [compare the intensity of CsPbBr<sub>2</sub><sup>+</sup> and CsPbBr<sub>3</sub><sup>+</sup> peaks in Fig. 2(a)], the presence of these components in the mass spectrum is indisputable proof that a congruent evaporation of CsPbBr3 occurs as well. However, the congruent evaporation is only a partial, although major, process. This is documented by the existence of Cs<sub>2</sub>Br<sup>+</sup>, which can hardly originate from the CsPbBr<sub>3</sub> molecular clusters alone. Its presence indicates that  $(CsBr)_x$  clusters evaporate as well  $(x \ge 2)$ .

Therefore, in addition to the congruent evaporation, the precursor in the crucible partially decomposes into CsBr and PbBr2, and these components evaporate (at different rates, see below) simultaneously with the congruently evaporated CsPbBr<sub>3</sub> [see Fig. 2(d)]. An extended analysis of KEMS data, including detailed temperature dependencies that further support these conclusions, is shown in the supplementary material (Figs. S4, S5, and S6). The equilibrium vapor pressure of PbBr<sub>2</sub> is higher as compared to that of CsBr; <sup>45,46</sup> therefore, if kept at the same temperature, PbBr<sub>2</sub> evaporates faster [compare the absolute ion currents in Figs. 2(b) and 2(c)]. This fact is also documented in Fig. 2(d), where the isothermal evaporation of CsPbBr<sub>3</sub> is monitored over time. The intensity of PbBr<sub>2</sub>-related ions decreases faster compared to those of CsBr. Therefore, the composition of the evaporant in the crucible gradually changes over time toward the Cs-rich phase. Consistent with the CsBr-PbBr<sub>2</sub> phase diagram,<sup>25</sup> when a certain stoichiometry is reached (ratio 4:1), the phase change of the evaporant to Cs<sub>4</sub>PbBr<sub>6</sub> occurs. This phase change is accompanied by different evaporation rates, followed by a rapid loss of PbBr-related components [clearly distinguishable in Fig. 2(d)]. Then, only CsBr is left within the crucible. Therefore, KEMS measurements explain the previous experimental findings reporting different evaporant compositions after growth runs. 26,4

Congruent evaporation typically occurs in nanocrystalline evaporants because the heat is delivered abruptly to the entire nanocrystal, leading to a rapid decomposition and evaporation. Therefore, the preparation method is expected to be important. Nevertheless, we have found that different forms of the evaporant produce very similar results (see supplementary material, Fig. S4). In addition, for evaporant temperatures between 400 and 450  $^{\circ}$ C, the vapor composition (ratios between components) is stable with the temperature (see Fig. S6). Therefore, if operated before the phase change to Cs<sub>4</sub>PbBr<sub>6</sub> and considering that vapor pressure depends on temperature, the single-source CsPbBr<sub>3</sub> evaporation also allows control of the deposition rate by adjusting the evaporant temperature.

Next, we show that it is possible to substantially tune the stoichiometry of the deposited layers by controlling the substrate temperature, without requiring extensive flux control. First, in Fig. 3, we show the XRD and SEM analyses of layers deposited from a single-source evaporant (CsPbBr<sub>3</sub>) at substrate temperatures ranging from room temperature (RT) to 250 °C. All growth runs were performed using a fresh evaporant at 450 °C to avoid changes in flux compositions due to phase changes in the evaporant [see Fig. 2(d)]. We observe that both the RT and 100 °C depositions yield a compact layer of CsPb<sub>2</sub>Br<sub>5</sub> (see Fig. 3). Upon increasing the substrate temperature, the grain size of the deposit slightly increases, while the nominal layer thickness corresponds to the deposition rate (470 nm). Conversely, we find that the morphology of the layer deposited at 200 °C is strikingly different. The individual grains possess a nearly cubic shape and, occasionally, nanowires of a rectangular cross section (up to 300 nm in size) and a maximum length of 2  $\mu$ m are protruding from the polycrystalline layer. We argue that the appearance of the layer is clearly related to the phase change. At 200 °C, an orthorhombic CsPbBr<sub>3</sub> phase is identified in the XRD spectra (see the left panel in Fig. 3 and Fig. S7 in the supplementary material for crystal phase identification) with only a very minor presence of Cs<sub>4</sub>PbBr<sub>6</sub>. At a higher sample temperature (250 °C), the fraction of Cs<sub>4</sub>PbBr<sub>6</sub> slightly increases. At even higher

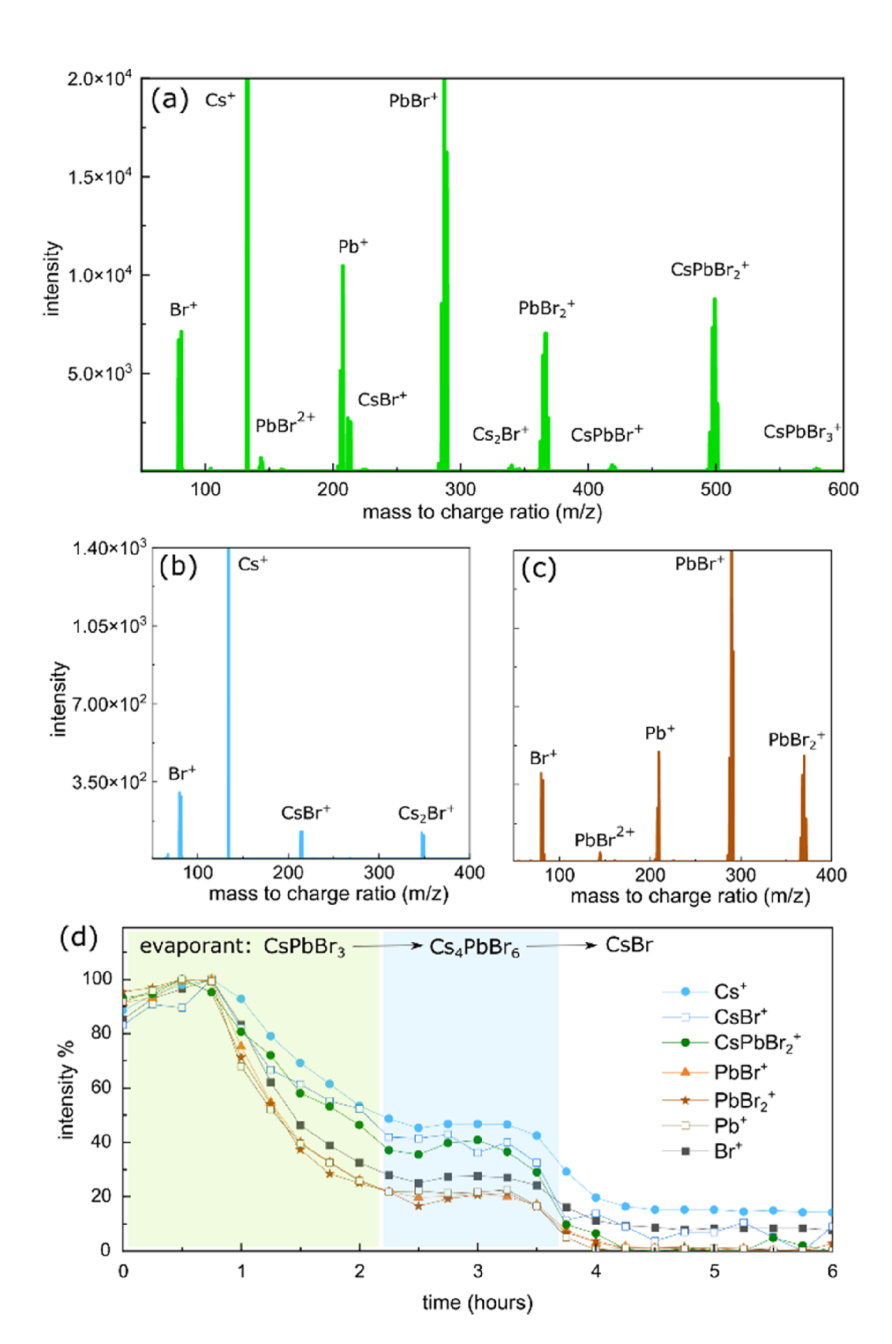


FIG. 2. KEMS results: Mass spectra of (a) CsPbBr<sub>3</sub> pellet held at 450 °C, (b) CsBr powder at 450 °C, (c) PbBr<sub>2</sub> powder at 300 °C. (d) Isothermal evaporation of the CsPbBr<sub>3</sub> evaporant at 450 °C, the most relevant components monitored in time (only selected components are shown for clarity; more data are in supplementary material, Fig. S3). The PbBr-related components are depleted faster (faster decrease in the graph for PbBr+, PbBr2+, Pb+, and Br+), and at a certain moment a phase change to Cs<sub>4</sub>PbBr<sub>6</sub> occurs. When all PbBr<sub>2</sub> evaporates, only CsBr remains.

temperature (300 °C, not shown), no layer is formed, as all deposited material is desorbed. Further analyses by XPS and Raman spectroscopy (see supplementary material, Figs. S8 and S9) support the phases identified by XRD.

The dual-source deposition (simultaneous independent evaporation of CsBr and PbBr<sub>2</sub>) allows tuning the PbBr<sub>2</sub>/CsBr flux ratio. Figure 4(a) shows XRD and SEM analyses of layers deposited at sample temperatures ranging from RT to 250 °C when the flux ratio is smaller than 1 (in this case, the PbBr<sub>2</sub>/CsBr flux ratio was 1:5). All the layers are composed mostly of CsBr. Only for lower sample temperatures (RT and 100 °C) is a certain fraction of Cs<sub>4</sub>PbBr<sub>6</sub> detected. As

expected, the grain size increases with temperature. At 250 °C, the layer is partially decomposed and roughened (similarly to the singlesource deposition). When the PbBr<sub>2</sub>/CsBr flux ratio is changed to 4:1 [Fig. 4(b)], the XRD analysis of perovskite phases resembles those of the single-source evaporation. The compact layer of CsPb<sub>2</sub>Br<sub>5</sub> is deposited at low temperatures (RT and 100 °C), while at higher temperatures, orthorhombic CsPbBr3 is formed. However, in contrast to the single-source evaporation, there are several noticeable differences. First, below 250 °C, the temperature is not high enough to evaporate excess PbBr<sub>2</sub>, as deduced from the PbBr<sub>2</sub> signatures in the XRD. Importantly, pure orthorhombic CsPbBr<sub>3</sub> is formed at 250 °C

APL Materials ARTICLE pubs.aip.org/aip/apm

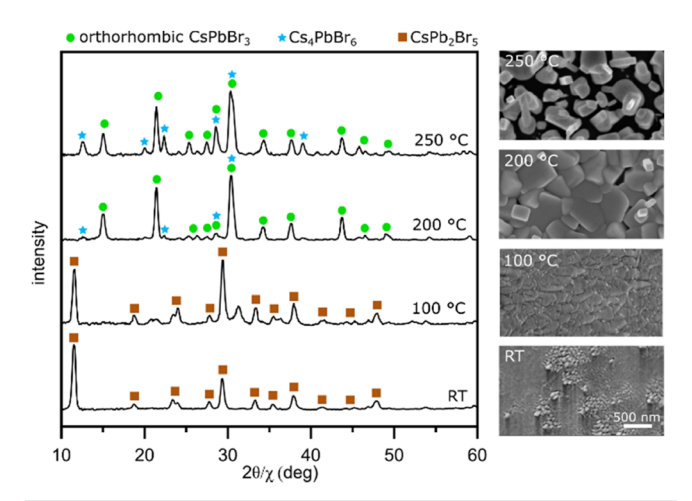


**FIG. 3.** Analysis of single-source (CsPbBr<sub>3</sub>, 450 °C, evaporation rate was 15 nm/min) deposited perovskite layers (30 min deposition) at different substrate temperatures (RT, 100, 200, and 250 °C). Peaks in XRD spectra are marked by symbols relevant for each phase: orthorhombic CsPbBr<sub>3</sub> ( ), CsPb<sub>2</sub>Br<sub>5</sub> ( ), and Cs<sub>4</sub>PbBr<sub>6</sub> ( ) (see Fig. S1 for the full spectra and detailed peak assignments). Representative SEM images of each sample are shown on the right.

(other phases were not detectable by XRD). At this temperature, the  $Cs_4PbBr_6$  present in samples prepared by the single-source evaporation is absent.  $CsPbBr_3$  deposited at 250  $^{\circ}C$  forms well-defined cuboid crystals as well as nanowires.

We have inspected the sample grown at 250 °C in more detail [see Fig. 5(a)]. The nanowires on the sample were all out-of-plane; no in-plane nanowires were observed. All the nanowires have a square cross section [see detail in Fig. 5(a)]. Interestingly, cuboid

crystals on the sample predominantly form near nanowires, appearing almost exclusively in their shadow along the direction of the PbBr<sub>2</sub> flux. The largest difference between the single- and dualsource evaporation is that using the latter approach, the growth of CsPbBr<sub>3</sub> is possible also at temperatures above 250 °C. In order to do so, the PbBr2/CsBr ratio has to be much higher compared to the one achievable by the single-source deposition. Figure 5(b) additionally shows that at 300 °C and under a very high PbBr<sub>2</sub> flux (PbBr<sub>2</sub>/CsBr flux ratio of 25:1), only small crystallites and relatively long CsPbBr3 nanowires are present on the surface. Interestingly, in contrast to the deposition at 250 °C, all the nanowires grow in-plane, along the substrate surface. In many cases, a small droplet is visible at the nanowire end [see the inset in the bottom panel of Fig. 5(b)], and the nanowires are frequently tapered. XRD revealed that both out-of-plane and in-plane oriented nanowires exhibit orthorhombic CsPbBr<sub>3</sub> structure (Fig. S7).

We have already demonstrated via XRD that dual-source deposition at sample temperatures above 200 °C produces better deposits in terms of phase purity. To support this conclusion with additional techniques, Fig. 6 illustrates the effects of x-ray exposure [Figs. 6(a)-6(c)], photoluminescence [PL, Fig. 6(d)], and timeresolved photoluminescence [TRPL, Fig. 6(e)] on the single-source deposited layer at 200 °C and the dual-source deposited samples (4:1 PbBr<sub>2</sub>:CsBr ratio) at 250 °C [refer to Figs. 3 and 4(b) for XRD and SEM images]. The degradation of halide perovskites under UV and x-ray radiation is a well-known effect.<sup>47</sup> The formation of metallic Pb after exposure to high-energy photons has been associated with PL quenching; subsequently, halide interstitials induce deep-level traps. 47 The former process is detectable through the emergence of a Pb<sup>0</sup> component (metallic Pb) in the XPS spectrum. The series of XPS measurements under continuous x-ray irradiation (1486 eV) shown in Fig. 6(c) indicates that the sample prepared by dualsource deposition exhibits negligible Pb<sup>0</sup> formation, in contrast to

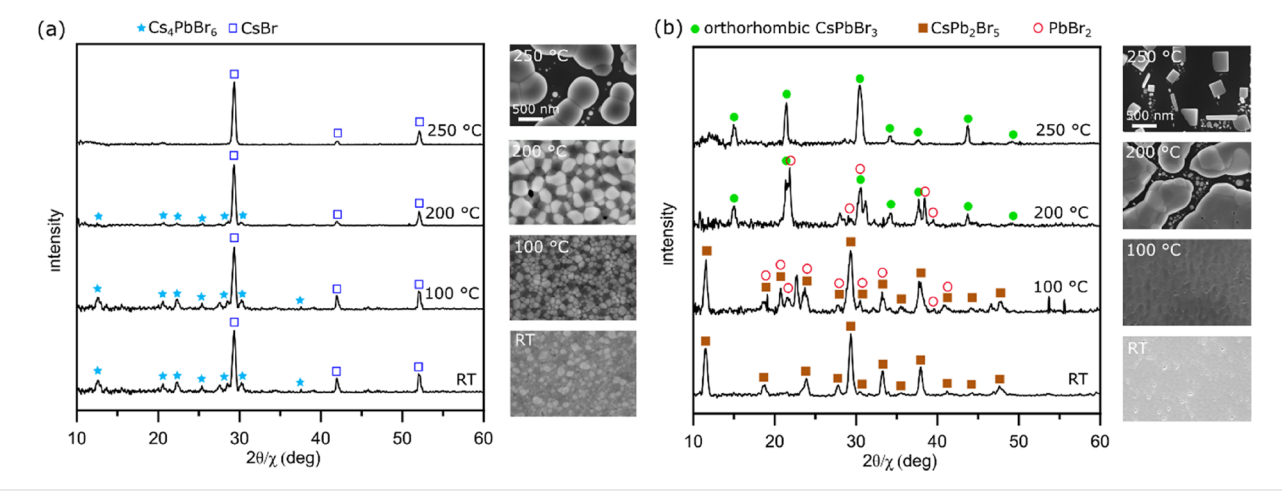


FIG. 4. Analysis of dual-source (CsBr and PbBr<sub>2</sub>) deposited perovskite layers at different sample temperatures (RT, 100, 200, 250 °C) and flux ratios. In (a), the XRD and SEM analyses of the layers deposited with a PbBr<sub>2</sub>/CsBr flux ratio of 1:5 is shown. The evaporator temperatures were 240 and 450 °C, providing absolute fluxes of 0.8 and 4 nm/min for PbBr<sub>2</sub> and CsBr, respectively. In (b), the same analysis is made for a PbBr<sub>2</sub>/CsBr flux ratio of 4:1. The evaporator temperatures were 300 and 400 °C, providing absolute fluxes of 8 and 2 nm/min for PbBr<sub>2</sub> and CsBr, respectively. Peaks in XRD spectra are marked by symbols relevant for each phase: orthorhombic CsPbBr<sub>3</sub> ( $\blacksquare$ ), CsPb<sub>2</sub>Br<sub>5</sub> ( $\blacksquare$ ), CsPbBr<sub>6</sub> (\*), CsBr ( $\square$ ), and PbBr<sub>2</sub> ( $\bigcirc$ ) (see Fig. S1 for the full spectra and detailed peak assignments).

APL Materials ARTICLE pubs.aip.org/aip/apm

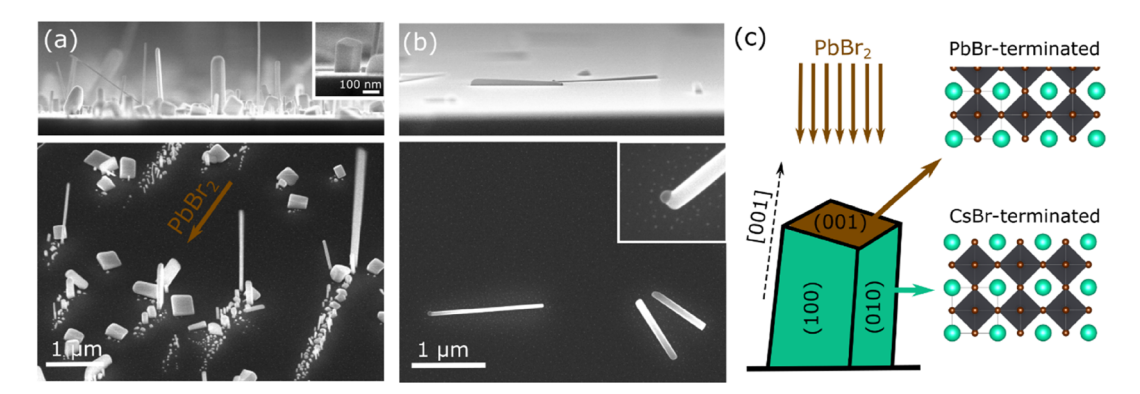
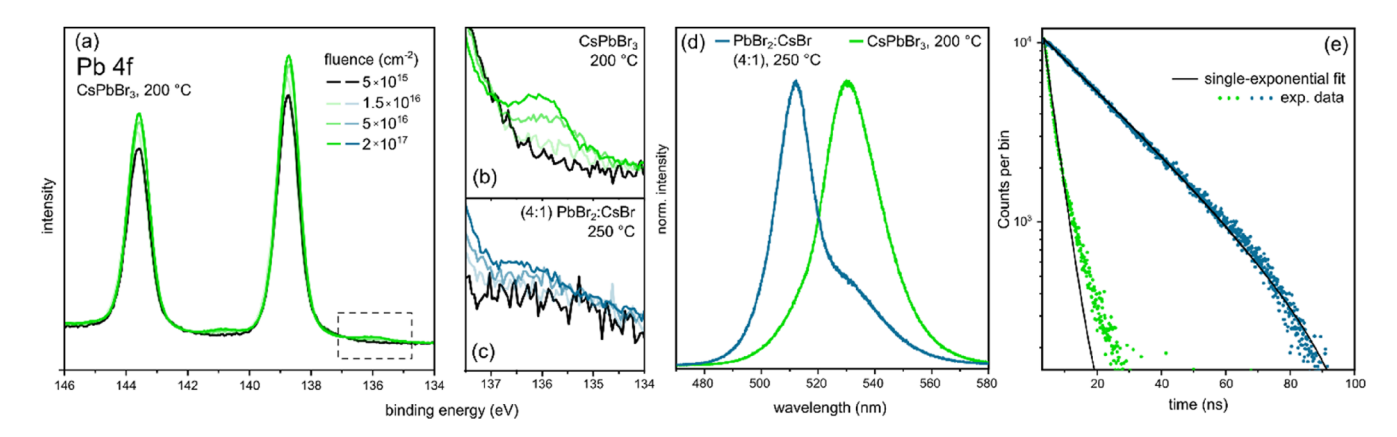


FIG. 5. CsPbBr<sub>3</sub> nanowires observed when higher substrate temperatures and PbBr<sub>2</sub> flux (dual source deposition) were used. In (a), a detailed SEM inspection of the sample grown at 250 °C [same as in Fig. 4(b), PbBr<sub>2</sub>/CsBr flux ratio of 4:1] is shown, with the side view in the top row and a tilted (45°) view in the bottom row. At 250 °C, out-of-plane CsPbBr<sub>3</sub> nanowires are formed, with cuboid CsPbBr<sub>3</sub> crystals mostly within the shade of nanowires in the direction of the PbBr<sub>2</sub> beam (the beam direction is marked by an arrow; the sample was not rotated during the evaporation). A SEM image of a slightly elongated cuboid crystal, with a clearly visible square top facet, which is identical to the nanowire cross section is shown in the inset. (b) The sample grown at 300 °C using a very high PbBr<sub>2</sub>/CsBr flux ratio of 25:1, where exclusively in-plane oriented CsPbBr<sub>3</sub> nanowires are formed. The evaporation temperatures were 360 and 400 °C, providing absolute fluxes of 50 and 2 nm/min for PbBr<sub>2</sub> and CsBr, respectively. The inset shows a detail of a nanowire tip with a nanoparticle, typical for vapor–solid–solid growth. (c) The schematic illustration shows the proposed model for anisotropic growth, including the side views of Cs–Br- and Pb–Br-terminated facets.

the single-source-deposited sample [Fig. 6(b)], where degradation is evident. It is worth noting, however, that the resistance of both samples to degradation under high-energy photon illumination is significantly greater when compared to samples composed of other perovskite phases (see Fig. S10). Deposits prepared using both deposition methods exhibit intense PL with peak maxima at positions characteristic of CsPbBr<sub>3</sub> [Fig. 6(d)].<sup>48</sup> The blueshift observed in the dual-source-deposited sample is attributed to quantum confinement effects in the nanowires and nanocubes present on the sample [see SEM images in Fig. 4(b)].<sup>48</sup> Despite two distinct charge carrier populations suggested by the PL spectra [Fig. 6(d), blue], the time-resolved PL decay of the dual-source-deposited sample [Fig. 6(e),

blue] can be fitted with a single exponential decay, suggesting an exciton lifetime of  $\tau_1$  = 24.8 ns and a photoluminescence quantum yield (PLQY) of 86%. Our current TRPL measurements lack wavelength selectivity. Therefore, we cannot distinguish between the two populations or determine specific recombination lifetimes for each charge carrier population in this sample individually. Nevertheless, the lifetime and PLQY observed in the dual-source-deposited sample are significantly higher compared to those of the single-source-deposited sample [Fig. 6(e), green,  $\tau_1$  = 3.4 ns, 13% PLQY]. In addition, in the latter case, the data deviate from a single exponential, suggesting the existence of an additional fast recombination channel, presumably caused by defect-mediated non-radiative decay.



**FIG. 6.** Comparison of optoelectronic properties of CsPbBr<sub>3</sub> prepared by different approaches (dual source, PbBr<sub>2</sub> + CsBr, 4:1, at 250 °C and single source, CsPbBr<sub>3</sub>, at 200 °C). Panel (a) shows the x-ray-induced damage evolution of the single-source deposited sample, documented by XPS spectra (in the Pb 4f region) after exposure to 1486 eV x-rays with an increasing fluence. A reduction of higher valence states of Pb to metallic Pb<sup>0</sup> is documented by the appearance of a component at 136 eV, which is shown in detail in (b). The same spectral detail is shown in (c) for the CsPbBr<sub>3</sub> sample grown by dual-source deposition after exposure to the same x-ray fluences. PL spectra and TRPL measurements of the two samples are shown in (d) and (e), respectively.

### **IV. DISCUSSION**

Comparing the results of single-source and dual-source deposition leads to the following conclusions. At low deposition temperatures, our results agree with those reported by previous studies; that is, both deposition approaches result in the CsPb2Br5 phase, occasionally mixed with CsPbBr<sub>3</sub>. In order to grow the pure CsPbBr<sub>3</sub> phase, one needs to raise the sample temperature. The KEMS data, together with the analyses shown in Figs. 3 and 4, allow us to explain the mechanism behind. An elevated sample temperature results in desorption of excess PbBr2 from the sample surface. This desorption of PbBr2 prevents the formation of the CsPb2Br5 phase at temperatures above 100 °C. Instead, at elevated sample temperatures, the growth rate becomes limited by the CsBr flux. This makes the CsPbBr3 growth mechanism on surfaces very similar to that of III-V semiconductor formation via molecular beam epitaxy: in excess of group V species, the growth is controlled by the group III element. Here, the large flux of PbBr2 allows the stoichiometric formation of CsPbBr3, while the elevated sample temperature ensures the desorption of excess PbBr<sub>2</sub>. This is valid for both the single-source and dual-source (with PbBr<sub>2</sub>/CsBr flux ratios >1) depositions. The PbBr<sub>2</sub>/CsBr flux ratio should be large; otherwise, the desorption of PbBr2 could be so fast that the growth of CsPbBr3 can become PbBr2-limited. This is the case of singlesource deposition at 250 °C (Fig. 3). In such a case, the lack of PbBr<sub>2</sub> (and, hence, the excess of CsBr) results in a partial formation of Cs<sub>4</sub>PbBr<sub>6</sub>. The desorption of PbBr<sub>2</sub> is a temperature-activated process, but the loss of PbBr2 at high temperatures can be compensated by a very large PbBr2 flux. This is achievable only through dual-source deposition enabling the growth of CsPbBr3 at sample temperatures exceeding 250 °C with very high purity, as demonstrated in Fig. 6. Notably, high-temperature deposition ensures the desorption of any unreacted PbBr<sub>2</sub>, efficiently eliminating PbBr<sub>2</sub> residues from the layer. Consequently, high-temperature-deposited layers exhibit higher photoluminescence quantum yield and longer exciton lifetimes. As shown in Figs. 4 and 5, increasing the sample temperature and providing a high PbBr2 flux causes the morphology of the CsPbBr3 deposit to rapidly change from a fairly compact layer to nanowires. The appearance of nanowires during the vapor phase deposition of inorganic perovskites at elevated temperatures has been observed previously. 19,24,49 This morphology change is still unexplored, despite attempts to explain it by temperature-dependent changes in the crystal structure.<sup>11</sup> Here, we observe two different cases. At the highest sample temperature of 300 °C inspected in this study (which is still below the liquidus line of the CsBr-PbBr2 phase diagram), Cs-Pb-Br alloy nanoparticles are formed that further collect the deposited species, facilitating onedimensional growth via the vapor-solid-solid (VSS) mechanism.<sup>50</sup> The appearance of nanoparticles at the tip of the nanowires is a typical signature of VSS growth. The in-plane nanowire geometry reached at this deposition temperature results from a nanoparticle movement on the surface during growth.<sup>51</sup> The nanoparticles shrink in time (and, potentially, fully diminish after some time), which is reflected in the tapered shape of the in-plane nanowires [Fig. 5(b), side view].

At the slightly lower sample temperature of 250 °C, but still under high PbBr<sub>2</sub> flux, the out-of-plane nanowires do not exhibit any nanoparticles at their tips. As the nanowire cross section does

not change along their axis, the absence of the droplet cannot be explained by its evaporation during growth. There is obviously another growth mechanism in play. We propose that the asymmetry promoting one-dimensional growth in the system is the distinct surface termination of CsPbBr3 facets. Cuboid CsPbBr3 crystals, as is the case here (Fig. 3), commonly exhibit (100) facets. 19 These facets are crystallographically identical, and under common growth conditions, they are Cs-Br terminated due to the lowest surface free energy of this termination. 52-54 We hypothesize that, at PbBr<sub>2</sub>-rich conditions, the facet that is most directly exposed to the incident flux transiently converts into a Pb-Br terminated one. Such a facet immediately develops into the fastest growing one due to an increase in the surface free energy.<sup>52</sup> As a result, cuboid crystals elongate along the [100] direction [Fig. 5(c)] and form nanowires with a square cross section, as observed experimentally [Fig. 5(a)]. The elevated growth temperatures promote the relevant kinetic processes (mostly surface diffusion), further accentuating the anisotropy of the growth.

For many device applications, phase-pure, continuous CsPbBr<sub>3</sub> layers are essential. Our data indicate a sample-temperaturedependent trade-off between phase purity and the continuity of vapor-deposited perovskite layers. The morphology of these layers can be further manipulated through various means. Polycrystalline layers, such as those prepared in this study, are commonly formed during the vapor deposition of perovskites.<sup>55</sup> The compactness of polycrystalline films improves with increased nucleation density,<sup>56</sup> which is critically influenced by the D/F ratio.<sup>30</sup> At low D/F ratios, the higher concentration of surface species increases the likelihood of stable nuclei formation, resulting in more compact films.<sup>56</sup> SEM images in Figs. 3 and 4(b) clearly illustrate this behavior: at constant flux F, low-temperature depositions (corresponding to low D/Fratios) result in more continuous films, whereas higher-temperature depositions (with higher D/F ratios) lead to predominantly isolated grains and nanowires. Therefore, phase-pure compact films can potentially be grown at elevated temperatures if the total flux *F* is significantly increased. Additional strategies to manipulate the growth mode include the appropriate choice of substrate (e.g., enabling epitaxial monocrystalline growth)<sup>57</sup> or the use of surfactants.<sup>30</sup> The former approach builds on the fact that diffusion is strongly straindependent, allowing the D/F ratio to be adjusted through substrate selection. The latter technique, widely used in homoepitaxy of metals,<sup>30</sup> has yet to be explored for the growth of inorganic perovskites. Both approaches merit further detailed investigation.

# V. CONCLUSIONS

In summary, we have demonstrated how differences in the vapor pressures of CsBr and PbBr<sub>2</sub> affect the vapor phase growth from both single- (CsPbBr<sub>3</sub>) and dual-sources (CsBr and PbBr<sub>2</sub>). Under an excess PbBr<sub>2</sub> flux, the growth of CsPbBr<sub>3</sub> is CsBr-limited. Hence, if growth is conducted at certain elevated sample temperatures, this mechanism allows full control of the growth rate by the CsBr flux in case of the dual-source deposition. Similarly, it allows the deposition of the pure CsPbBr<sub>3</sub> phase. Our study shows that both single- and dual-source depositions of inorganic perovskites may result in layers with a prevailing CsPbBr<sub>3</sub> phase if appropriately controlled. However, single-source deposition requires caution; longer operation results in a phase change of the evaporant and related flux variations. In addition, the dual-source deposition is more flexible

because it allows tuning the fluxes of each component independently. The ability to independently increase the PbBr $_2$  flux is critical for phase-pure deposition of CsPbBr $_3$ , as phase purity improves with sample temperature during deposition, provided that sufficient PbBr $_2$  flux is supplied. This has been demonstrated through XRD and PL measurements. Flux variations broaden the variety of CsPbBr $_3$  morphologies, ranging from cubic nanoparticles to nanowires. We have proposed a nanowire formation mechanism specific for CsPbBr $_3$  that explains the nanowire growth at high temperatures via changes in the surface-termination of the top facet under an excessive PbBr $_2$  flux.

## SUPPLEMENTARY MATERIAL

See the supplementary material for reference XRD data, a description of the Knudsen effusion mass spectrometer, additional KEMS data, additional XRD analysis, XPS analysis of the deposits, Raman spectrum of the CsPb<sub>2</sub>Br<sub>5</sub> phase, and additional references.

### **ACKNOWLEDGMENTS**

This article is partially based on work from COST Action OPERA—European Network for Innovative and Advanced Epitaxy—CA20116, supported by COST (European Cooperation in Science and Technology, <a href="https://www.cost.eu">www.cost.eu</a>). The CzechNanoLab Project No. LM2023051 funded by MEYS CR is gratefully acknowledged for providing financial support for the measurements at the CEITEC Nano Research Infrastructure. This work was supported by the project Quantum Materials for Applications in Sustainable Technologies (QM4ST), funded as Project No. CZ.02.01.01/00/22\_008/0004572 by OP JAK, call Excellent Research, and the authors also acknowledge funding by Specific Research of BUT FCH/FSI-J-24-8514. We acknowledge Martin Kovařík for the AFM analysis of the layers.

# **AUTHOR DECLARATIONS**

# **Conflict of Interest**

The authors have no conflicts to disclose.

# **Author Contributions**

Tomáš Musálek: Conceptualization (equal); Formal analysis (equal); Investigation (lead); Methodology (equal); Writing – original draft (supporting); Writing – review & editing (equal). Petr Liška: Formal analysis (equal); Investigation (equal); Writing – review & editing (equal). Amedeo Morsa: Formal analysis (equal); Investigation (equal); Writing – review & editing (equal). Jon Ander Arregi: Formal analysis (equal); Investigation (equal); Writing – review & editing (equal). Pavel Klok: Investigation (equal); Writing – review & editing (equal). Matouš Kratochvíl: Investigation (equal); Writing – review & editing (equal). Dmitry Sergeev: Formal analysis (equal); Investigation (equal); Writing – review & editing (equal). Michael Müller: Conceptualization (equal); Writing – review & editing (equal). Tomáš Šikola: Supervision (equal); Writing – review & editing (equal). Miroslav Kolíbal: Conceptualization

(equal); Formal analysis (equal); Investigation (equal); Methodology (equal); Supervision (lead); Writing – original draft (lead); Writing – review & editing (equal).

### **DATA AVAILABILITY**

The data that support the findings of this study are openly available in Zenodo, at https://doi.org/10.5281/zenodo.13880632, reference number 13880632.

#### **REFERENCES**

- <sup>1</sup>J. Luo, J. Li, L. Grater, R. Guo, A. R. bin Mohd Yusoff, E. Sargent, and J. Tang, Nat. Rev. Mat. **9**, 282 (2024).
- <sup>2</sup> A. Rao, M. Shin, Y. Lee, H. Kang, J. Han, M. Kim, S. Jo, J. H. Kim, and S. H. Cho, Nano Lett. **24**, 7717 (2024).
- <sup>3</sup>L. Protesescu, S. Yakunin, M. I. Bodnarchuk, F. Krieg, R. Caputo, C. H. Hendon, R. X. Yang, A. Walsh, and M. V. Kovalenko, Nano Lett. 15, 3692 (2015).
- <sup>4</sup>B. Schwarz, P. Reininger, H. Detz, T. Zederbauer, A. Maxwell Andrews, S. Kalchmair, W. Schrenk, O. Baumgartner, H. Kosina, and G. Strasser, Appl. Phys. Lett. **101**, 191109 (2012).
- <sup>5</sup>P. Zeng, Y. Wang, Q. Zhang, Y. Yang, J. Gong, G. Feng, and M. Liu, J. Phys. Chem. Lett. 14, 4638 (2023).
- <sup>6</sup>T. Soto-Montero, W. Soltanpoor, and M. Morales-Masis, APL Mater. **8**, 111108 (2020).
- <sup>7</sup>S. Bonomi and L. Malavasi, J. Vac. Sci. Technol., A 38, 063407 (2020).
- <sup>8</sup>Q. Guesnay, F. Sahli, C. Ballif, and Q. Jeangros, APL Mater. **9**, 100901 (2021).
- <sup>9</sup>M. Shin, H. S. Lee, Y. C. Sim, Y. H. Cho, K. Cheol Choi, and B. Shin, ACS Appl. Mater. Interfaces 12, 1944 (2020).
- <sup>10</sup>I. J. Cleveland, M. N. Tran, A. Dey, and E. S. Aydil, J. Vac. Sci. Technol., A 39, 043403 (2021).
- <sup>11</sup> H. Zhou, S. Yuan, X. Wang, T. Xu, X. Wang, H. Li, W. Zheng, P. Fan, Y. Li, L. Sun, and A. Pan, ACS Nano 11, 1189 (2017).
- <sup>12</sup>M. Liu, M. B. Johnston, and H. J. Snaith, Nature **501**, 395 (2013).
- <sup>13</sup> J. Li, P. Du, Q. Guo, L. Sun, Z. Shen, J. Zhu, C. Dong, L. Wang, X. Zhang, L. Li, C. Yang *et al.*, Nat. Photonics **17**, 435 (2023).
- <sup>14</sup>Y. Hu, Q. Wang, Y. L. Shi, M. Li, L. Zhang, Z. K. Wang, and L. S. Liao, J. Mater. Chem. C 5, 8144 (2017).
- <sup>15</sup>C. P. Clark, B. Voigt, E. S. Aydil, and R. J. Holmes, Sustainable Energy Fuels 3, 2447 (2019).
- <sup>16</sup>S. Sanders, D. Stümmler, P. Pfeiffer, N. Ackermann, G. Simkus, M. Heuken, P. K. Baumann, A. Vescan, and H. Kalisch, Sci. Rep. 9, 9774 (2019).
- <sup>17</sup>U. Bansode, R. Naphade, O. Game, S. Agarkar, and S. Ogale, J. Phys. Chem. C 119, 9177 (2015).
- <sup>18</sup>W. A. Dunlap-Shohl, E. T. Barraza, A. Barrette, K. Gundogdu, A. D. Stiff-Roberts, and D. B. Mitzi, ACS Energy Lett. 3, 270 (2018).
- <sup>19</sup>Y. Wang, X. Sun, R. Shivanna, Y. Yang, Z. Chen, Y. Guo, G. C. Wang, E. Wertz, F. Deschler, Z. Cai, H. Zhou *et al.*, Nano Lett. **16**, 7974 (2016).
- $^{\bf 20}$  M. Era, T. Hattori, T. Taira, and T. Tsutsui, Chem. Mater.  $\bf 9, 8$  (1997).
- <sup>21</sup> L. A. Frolova, D. V. Anokhin, A. A. Piryazev, S. Y. Luchkin, N. N. Dremova, K. J. Stevenson, and P. A. Troshin, J. Phys. Chem. Lett. 8, 67 (2017).
- <sup>22</sup>Q. Ma, S. Huang, X. Wen, M. A. Green, and A. W. Y. Ho-Baillie, Adv. Energy Mater. 6, 1502202 (2016).
- <sup>23</sup> J. Chen, Y. Fu, L. Samad, L. Dang, Y. Zhao, S. Shen, L. Guo, and S. Jin, Nano Lett. 17, 460 (2017).
- <sup>24</sup> X. Mo, X. Li, G. Dai, P. He, J. Sun, H. Huang, and J. Yang, Nanoscale 11, 21386 (2019).
- <sup>25</sup> A. Ishteev, L. Luchnikov, D. S. Muratov, M. Voronova, A. Forde, T. Inerbaev, V. Vanyushin, D. Saranin, K. Yusupov, D. Kuznetsov, and A. Di Carlo, Appl. Phys. Lett. 119, 071901 (2021).
- <sup>26</sup> J. Li, R. Gao, F. Gao, J. Lei, H. Wang, X. Wu, J. Li, H. Liu, X. Hua, and S. F. Liu, J. Alloys Compd. 818, 152903 (2020).
- <sup>27</sup>Y. Ling, L. Tan, X. Wang, Y. Zhou, Y. Xin, B. Ma, K. Hanson, and H. Gao, J. Phys. Chem. Lett. 8, 3266 (2017).

- <sup>28</sup>C. Chen, T. H. Han, S. Tan, J. Xue, Y. Zhao, Y. Liu, H. Wang, W. Hu, C. Bao, M. Mazzeo, R. Wang *et al.*, Nano Lett. **20**, 4673 (2020).
- <sup>29</sup> J. V. Barth, G. Costantini, and K. Kern, Nature **437**(7059), 671–679 (2005).
- <sup>30</sup>H. Brune, Surf. Sci. Rep. **31**, 125 (1998).
- <sup>31</sup> C. Qiu, A. Dumont, P. Li, and Z. H. Lu, Adv. Photonics Res. 2, 2000140 (2021).
- <sup>32</sup>S. Cheng, Y. Lee, J. Yu, L. Yu, and M. D. Ediger, J. Phys. Chem. Lett. **14**, 4297 (2023).
- <sup>33</sup> M. Shahiduzzaman, K. Yonezawa, K. Yamamoto, T. S. Ripolles, M. Karakawa, T. Kuwabara, K. Takahashi, S. Hayase, and T. Taima, ACS Omega 2, 4464 (2017).
- <sup>34</sup>Y. Zhang, L. Luo, J. Hua, C. Wang, F. Huang, J. Zhong, Y. Peng, Z. Ku, and Y. B. Cheng, Mater. Sci. Semicond. Process. 98, 39 (2019).
- <sup>35</sup>H. Li, G. Tong, T. Chen, H. Zhu, G. Li, Y. Chang, L. Wang, and Y. Jiang, J. Mater. Chem. A 6, 14255 (2018).
- <sup>36</sup>N. Chand, J. Cryst. Growth **97**, 415 (1989).
- <sup>37</sup>J. R. Chin, M. B. Frye, D. S. H. Liu, M. Hilse, I. C. Graham, J. Shallenberger, K. Wang, R. Engel-Herbert, M. Wang, Y. K. Shin, N. Nayir *et al.*, Nanoscale **15**, 9973 (2023).
- <sup>38</sup>L. Harris and B. M. Siegel, J. Appl. Phys. **19**, 739 (1948).
- <sup>39</sup> J. L. Richards, P. B. Hart, and L. M. Gallone, J. Appl. Phys. **34**, 3418 (1963).
- <sup>40</sup> A. Kanak, O. Kopach, L. Kanak, I. Levchuk, M. Isaiev, C. J. Brabec, P. Fochuk, and Y. Khalavka, Cryst. Growth Des. 22, 4115 (2022).
- <sup>41</sup>Y. El Ajjouri, F. Palazon, M. Sessolo, and H. J. Bolink, Chem. Mater. **30**, 7423 (2018).
- <sup>42</sup>L. Nasi, D. Calestani, F. Mezzadri, F. Mariano, A. Listorti, P. Ferro, M. Mazzeo, and R. Mosca, Front. Chem. 8, 313 (2020).
- <sup>43</sup>V. I. Nefedov, J. Electron Spectrosc. Relat. Phenom. 25, 29 (1982).
- <sup>44</sup>I. W. Drummond, in *Surface Analysis by Auger and X-Ray Photoelectron Spectroscopy*, edited by D. Briggs and J. T. Grant (IM Publications, Chichester, 2003), pp. 117–144.

- <sup>45</sup>K. Hilpert, M. Miller, A. Feltrin, and Schr. Forschungszent. Juelich, Reihe Energietech./Energy Technol. 15, 463 (2000).
- <sup>46</sup> A. Iizuka, E. Shibata, M. Sato, and T. Nakamura, Thermochim. Acta 622, 103 (2015).
- <sup>47</sup> J. Holovský, A. Peter Amalathas, L. Landová, B. Dzurnák, B. Conrad, M. Ledinský, Z. Hájková, O. Pop-Georgievski, J. Svoboda, T. C. J. Yang, and Q. Jeangros, ACS Energy Lett. 4, 3011 (2019).
- <sup>48</sup> P. Liška, T. Musálek, T. Šamořil, M. Kratochvíl, R. Matula, M. Horák, M. Nedvěd, J. Urban, J. Planer, K. Rovenská, P. Dvořák *et al.*, J. Phys. Chem. C **127**, 12404 (2023)
- <sup>49</sup>Y. Meng, C. Lan, F. Li, S. Yip, R. Wei, X. Kang, X. Bu, R. Dong, H. Zhang, and J. C. Ho, ACS Nano 13, 6060 (2019).
- <sup>50</sup>Y. Wang, V. Schmidt, S. Senz, and U. Gösele, Nat. Nanotechnol. 1, 186 (2006).
- 51 A. Rothman, K. Bukvišová, N. R. Itzhak, I. Kaplan-Ashiri, A. E. Kossoy, X. Sui, L. Novák, T. Šikola, M. Kolíbal, and E. Joselevich, ACS Nano 16, 18757 (2022).
- <sup>52</sup>Y. Yang, C. Hou, and T. X. Liang, Phys. Chem. Chem. Phys. **23**, 7145 (2021).
- <sup>53</sup>F. Bertolotti, G. Nedelcu, A. Vivani, A. Cervellino, N. Masciocchi, A. Guagliardi, and M. V. Kovalenko, ACS Nano 13, 14294 (2019).
- <sup>54</sup>Y. Chen, S. R. Smock, A. H. Flintgruber, F. A. Perras, R. L. Brutchey, and A. J. Rossini, J. Am. Chem. Soc. **142**, 6117 (2020).
- <sup>55</sup>V. Held, N. Mrkyvkova, Y. Halahovets, P. Nádaždy, K. Vegso, A. Vlk, M. Ledinský, M. Jergel, S. Bernstorff, J. Keckes, F. Schreiber, and P. Siffalovic, ACS Appl. Mater. Interfaces 16, 35723 (2024).
- <sup>56</sup>I. V. Markov, Crystal Growth for Beginners: Fundamentals of Nucleation, Crystal Growth and Epitaxy (World Scientific, 2016).
- <sup>57</sup>S. Liu, Y. Chen, W. Gao, W. Li, X. Yang, Z. Li, Z. Xiao, Y. Liu, and Y. Wang, Adv. Mater. 35(31), 2303544 (2023).